Editors' Suggestion

Dynamics of an itinerant spin-3 atomic dipolar gas in an optical lattice

Petra Fersterer,[1,2] Arghavan Safavi-Naini,[3,4] Bihui Zhu,[5,6] Lucas Gabardos,[7,8] Steven Lepoutre,[7,8] L. Vernac,[7,8] B. Laburthe-Tolra,[7,8] P. Blair Blakie,[1,2] and Ana Maria Rey[3,9]

[1]*The Dodd-Walls Centre for Photonic and Quantum Technologies, Dunedin 9054, New Zealand*
[2]*Department of Physics, University of Otago, Dunedin 9016, New Zealand*
[3]*JILA, NIST, and Department of Physics, University of Colorado, 440 UCB, Boulder, Colorado 80309, USA*
[4]*Centre for Engineered Quantum Systems, School of Mathematics and Physics, The University of Queensland, St Lucia, Queensland 4072, Australia*
[5]*ITAMP, Harvard-Smithsonian Center for Astrophysics, Cambridge, Massachusetts 02138, USA*
[6]*Department of Physics, Harvard University, Cambridge, Massachusetts 02138, USA*
[7]*Université Paris 13, Université Sorbonne Paris Cité, Laboratoire de Physique des Lasers, F-93430 Villetaneuse, France*
[8]*CNRS, UMR 7538, LPL, F-93430 Villetaneuse, France*
[9]*Center for Theory of Quantum Matter, University of Colorado, Boulder, Colorado 80309, USA*

(Received 20 May 2019; published 10 September 2019)

Arrays of ultracold dipolar gases loaded in optical lattices are emerging as powerful quantum simulators of the many-body physics associated with the rich interplay between long-range dipolar interactions, contact interactions, motion, and quantum statistics. In this work we report on our investigation of the quantum many-body dynamics of a large ensemble of bosonic magnetic chromium atoms with spin $S = 3$ in a three-dimensional lattice as a function of lattice depth. Using extensive theory and experimental comparisons, we study the dynamics of the population of the different Zeeman levels and the total magnetization of the gas across the superfluid to the Mott insulator transition. We are able to identify two distinct regimes. At low lattice depths, where atoms are in the superfluid regime, we observe that the spin dynamics is strongly determined by the competition between particle motion, on-site interactions, and external magnetic-field gradients. Contact spin-dependent interactions help to stabilize the collective spin length, which sets the total magnetization of the gas. On the contrary, at high lattice depths, transport is largely frozen out. In this regime, while the spin populations are mainly driven by long-range dipolar interactions, magnetic-field gradients also play a major role in the total spin demagnetization. We find that the dynamics at low lattice depth is qualitatively reproduced by mean-field calculations based on the Gutzwiller ansatz; on the contrary, only a beyond-mean-field theory can account for the dynamics at large lattice depths. While the crossover between these two regimes does not display sharp features in the observed dynamical evolution of the spin components, our simulations indicate that it would be better revealed by measurements of the collective spin length.

DOI: 10.1103/PhysRevA.100.033609

I. INTRODUCTION

Ultracold gases provide an excellent platform to study strongly correlated out-of-equilibrium quantum matter. So far, a broad range of atomic, molecular, and optical systems [1–3] including trapped ions [4–7] polar molecules [8,9], Rydberg atoms [10–14], magnetic atoms [15–21], and cavity QED arrays [22,23] has been used to realize quantum many-body systems with long-range interactions and to probe equilibrium properties and out-of-equilibrium dynamics in both pinned and itinerant systems.

Magnetic atoms trapped in optical lattices [24] naturally form a quantum simulator for complex $S > 1/2$ models due to the exponential growth in Hilbert space [25,26]. In these systems, the large number of spin degrees of freedom, as well as the ability to create lattices with itinerant particles, where neither motional nor interaction effects can be neglected, quickly limits the capability of current state-of-the-art numerical methods to tackle the complex quantum dynamics. The high level of control and tunability in these simulation platforms has already resulted in numerous pioneering experiments in three-dimensional (3D) optical lattices. These include studies of extended Bose-Hubbard models [16] and spin lattice models [27] with erbium atoms using $S = 6$ bosonic and $F = 19/2$ fermionic isotopes, respectively, as well as the spin dynamics of $S = 3$ bosonic chromium (^{52}Cr) atoms in both the superfluid and the Mott insulator regimes [15,17,18].

In this work we present experimental results together with an extensive numerical study of the spin dynamics seen in an array of bosonic ^{52}Cr atoms in a 3D lattice. By tuning the lattice depth, we explore the itinerant regime, where spin dynamics and tunneling occur over similar timescales. This regime is expected to be the most relevant for quantum simulations, since the complexity is then such that exact calculations are intractable by classical computers. We focus on lattice depths that span the Mott insulator to superfluid transition. The dynamics is initialized by rapidly rotating a fully polarized equilibrium state, initially pointing in the magnetic-field direction, to orient the atomic spins in a direction perpendicular to the magnetic field, corresponding to

a coherent superposition of all the magnetic sublevels. The system is then left to freely evolve at a fixed lattice depth. A residual magnetic-field gradient and both dipolar and contact interactions generate spin dynamics beyond the expected simple spin precession. Notably, the populations of the seven different Zeeman sublevels are observed to evolve following the spin rotation in a nontrivial way. We also investigate theoretically the dynamics of the total magnetization (i.e., collective spin length) of the gas which tends to decay as the system evolves.

Through our theoretical analysis we find that the system dynamics falls into two general regimes of behavior. (i) At low lattice depths, where the system is in the superfluid regime, spin transport is important as the gradient field drives the magnetic sublevels to spatially separate. The spin dynamics happens in a way that is strongly affected by the on-site interactions. We develop a mean-field Gutzwiller model [28,29] to study this regime. The Gutzwiller model is able to qualitatively describe the experimentally observed population dynamics as well as the inhibition of the demagnetization process due to the spin-dependent on-site interactions. This is similar to the protection against demagnetization and the persistence of ferromagnetic textures induced by the spin-dependent contact interactions recently observed in a Bose-Einstein condensate in a dipole trap [30]. (ii) In deeper lattices transport is inhibited as the system enters the Mott insulator regime. Here the dynamics of spin populations are driven primarily by long-range dipolar interactions. We use a generalized discrete truncated Wigner approximation (GDTWA) [15,31–33] to describe the dynamics in this frozen-atom regime. Similar observations were reported before at deep lattices [15]; however, what is surprisingly observed in this study is that the spin population dynamics remains almost independent of the lattice depth as the system approaches the Mott insulating regime and that we are able to reproduce well the observed dynamics using the GDTWA method over a broad range of lattice depths.

The Gutzwiller method predicts a strong reduction of spin dynamics as the lattice is raised and crosses the transition to the Mott insulating state. However, this is at odds with the experimental data, where a pronounced signature of the underlying quantum critical point in the spin population dynamics is absent. We attribute this to the quantum fluctuations which are not taken into consideration in the Gutzwiller treatment. Instead of the abrupt change obtained within the Gutzwiller approach, what is observed is a gradual change between the two previously studied regimes: a classical ferrofluid without lattices [34] and a correlated spin model at large lattice depths [15]. We note that a clearer signature of the transition appears in the theoretically calculated spin length, which we expect could be measured in future experiments.

The paper is structured as follows. We discuss the experimental system and introduce the corresponding generalized Bose-Hubbard model that describes the dynamics. We then introduce the Gutzwiller and the GDTWA methods and present the results of a second-order perturbative treatment of the spin dynamics. Next we study the dynamics starting from a simplified two-site model, which can be simulated exactly. We use the two-site model to identify key processes and to also benchmark the validity of the Gutzwiller approximation and the perturbative treatments. We then use the different numerical approaches to model the experimentally observed population dynamics at various lattice depths. We also study the dynamics of the collective spin length (i.e., the dynamical evolution of the total magnetization). We use both the populations and magnetization dynamics to look for signatures of the superfluid to Mott insulator transition and to understand the underlying physics in the two regimes.

II. SYSTEM AND HAMILTONIAN

Chromium atoms are loaded into a 3D optical lattice as illustrated schematically in Fig. 1 and described by the lattice vectors $\{\mathbf{u}_X, \mathbf{u}_Y, \mathbf{u}_Z\}$. The lattice depth along each of the three lattice vectors is proportional to V_0. The spatial extent of the system is determined by the harmonic confinement $\mathcal{V}_{\rm tr} = \frac{1}{2}m\sum_{\alpha=x,y,z}\omega_\alpha^2 x_\alpha^2$ and the total number of atoms $N \approx 3\times 10^4$. The spin degree of freedom is encoded in the Zeeman sublevels of the $S=3$ ground state of the ^{52}Cr atoms (see the inset to Fig. 1). An external magnetic field in the direction $\hat{\mathbf{B}}$ sets the quantization axis. This field has a bias value of 380 mG with the gradient lying approximately along the $\mathbf{u}_Z$ direction (see the inset to Fig. 1).

In the tight-binding regime chromium atoms in the lowest band of the optical lattice are modeled as occupying Wannier state spatial orbitals $W(\mathbf{r}-\mathbf{r}_i)$, centered on each lattice site $\mathbf{r}_i$. Here we consider the lattice site index $i=(i_X, i_Y, i_Z)$ a triad of integers such that $\mathbf{r}_i = \sum_{\alpha=X,Y,Z} i_\alpha \mathbf{u}_\alpha$. The dynamics of our system is described by the generalized Bose-Hubbard model

$$\begin{aligned}\hat{H} = &-\sum_{\alpha=X,Y,Z} J_\alpha \sum_{\langle i,j\rangle_\alpha}\sum_m \hat{a}^\dagger_{m,i}\hat{a}_{m,j} + \sum_i \mathcal{V}_{\rm tr}(\mathbf{r}_i)\hat{N}_i \\ &+ q\sum_j\sum_m m^2\hat{N}_{mj} - \gamma_B\sum_i b(\mathbf{r}_i)\sum_{mn} S^z_{mn}\hat{a}^\dagger_{m,i}\hat{a}_{n,i} \\ &+ \frac{1}{2}\sum_{m,m',n,n'}\sum_i C^{mm'nn'}\hat{a}^\dagger_{m,i}\hat{a}^\dagger_{m',i}\hat{a}_{n',i}\hat{a}_{n,i} \\ &+ \frac{1}{2}\sum_{m,m',n,n'}\sum_{i,j} D^{mm'nn'}_{ij}\hat{a}^\dagger_{m,i}\hat{a}^\dagger_{m',j}\hat{a}_{n',j}\hat{a}_{n,i}, \end{aligned} \tag{1}$$

where the indices m, m', n, n' label the Zeeman sublevels of the atoms and $\langle\cdots\rangle_\alpha$ is used to indicate nearest neighbors along the direction $\mathbf{u}_\alpha$, with J_α the tunneling amplitude in this direction. The operator $\hat{a}_{m,j}$ ($\hat{a}^\dagger_{m,j}$) destroys (creates) a spin-3 bosonic particle in the m Zeeman sublevel at site j, $\hat{N}_{mj} = \hat{a}^\dagger_{m,j}\hat{a}_{m,j}$, and the total number of atoms on each site is given by $\hat{N}_j = \sum_m \hat{N}_{mj}$. The constant part of the bias field is removed by working in the rotating frame. In this frame the terms in the Hamiltonian that do not preserve the total magnetization are rotated out and only the terms that preserve it are retained. The remaining contribution from the external field is the gradient term described by $b(\mathbf{r}) \approx b\mathbf{r}\cdot\mathbf{u}_Z$, with $S^{x,y,z}_{mn}$ the x, y, z components of the spin-3 matrices, respectively, and $\gamma_B = g\mu_B/\hbar$, where $g \simeq 2$ is the Landé g factor and μ_B is the Bohr magneton. The atoms also experience an effective quadratic Zeeman energy shift q that arises from tensorial light shifts

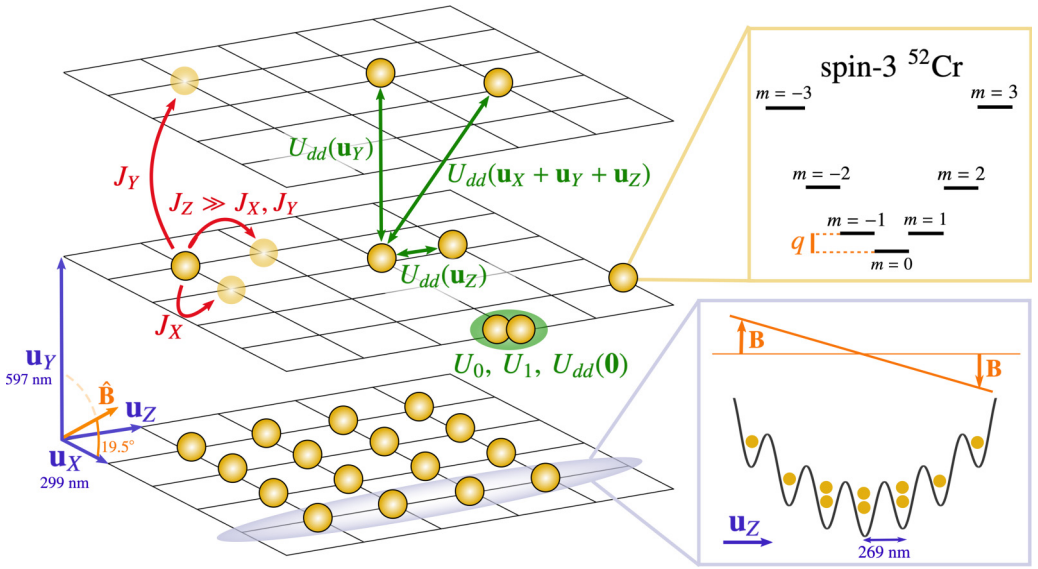

FIG. 1. Schematic of the system diagram indicating the 3D geometry of the optical lattice, the interactions, and tunneling processes. The magnetic field (with direction $\hat{\mathbf{B}}$ in the $\mathbf{u}_X$-$\mathbf{u}_Y$ plane) has a gradient lying along the $\mathbf{u}_Z$ direction (lower inset). Each spin-3 chromium atom also has its sublevels shifted by a quadratic Zeeman term (upper inset).

of the atomic levels.[1] The quadratic Zeeman energy q varies with the lattice depth (see, e.g., Ref. [15]).

The last two terms in the Hamiltonian (1) describe the interactions. The contact interaction is of the form [35]

$$C^{mm'nn'} = U_0 \delta_{m,n}\delta_{m',n'} + U_1 \sum_{\alpha} S^{\alpha}_{mn} S^{\alpha}_{m'n'}, \tag{2}$$

where $U_n = \tilde{c}_n \int d\mathbf{r} |W(\mathbf{r})|^4$. The contact interaction can also include higher-order spin terms (for the full form see Appendix B), but for the states accessible during the dynamics in consideration these have negligible effect compared to the contributions from the U_0 and U_1 terms. Finally, the dipole-dipole interactions (DDI) are described by (see [36])

$$D_{ij}^{mm'nn'} = \left(\tfrac{1}{2} S^x_{mn} S^x_{m'n'} + \tfrac{1}{2} S^y_{mn} S^y_{m'n'} - S^z_{mn} S^z_{m'n'}\right) \times U_{dd}(\mathbf{r}_i - \mathbf{r}_j), \tag{3}$$

where

$$U_{dd}(\mathbf{R}) = \frac{4\pi}{3} c_{dd} \mathcal{F}^{-1}\left[\left(1 - 3\frac{(\mathbf{k}\cdot\hat{\mathbf{B}})^2}{k^2}\right)\mathcal{F}(|W(\mathbf{r})|^2)^2\right] \tag{4}$$

is the kernel of the time-averaged (due to the rapid precession of the spin moments in the bias field) DDI between atoms in Wannier states separated by distance $\mathbf{R}$, with $c_{dd} = \mu_0 (g\mu_B)^2/4\pi$. Here we have used $\mathcal{F}$ and $\mathcal{F}^{-1}$ to denote the Fourier transform and its inverse, respectively. Because the DDIs decay rapidly with spatial separation, we restrict the summation to pairs of particles separated by up to one lattice site in each direction. This restriction reduces the computational difficulty and we find that it does not affect the main results of our paper, as long as only a qualitative agreement is sought.

[1]Because ^{52}Cr has no hyperfine structure, the magnetic field does not create a quadratic Zeeman effect.

To understand the system dynamics it is important to quantify the many microscopic parameters of the system which appear in the Hamiltonian. We summarize these values for three cases of the lattice depth V_0 in Table I. We note that the 3D lattice considered here is nonseparable and we approximate the Wannier functions of the ground band as Gaussians in order to obtain estimates of the interaction terms $\{U_0, U_{dd}(\mathbf{R})\}$. The initial distribution of the atoms in the lattice depends on lattice depth because it varies the strength of the on-site interactions (U_n) but also because the focused lasers used to make the lattice contribute to the harmonic confinement which increases with lattice depth.

In our experiments an initial state is produced by loading a Bose-Einstein condensate of Cr atoms spin polarized in the

TABLE I. Parameters for different lattice depths V_0 measured in units of the recoil energy E_r for $\lambda = 532$ nm. Here ω_z is the estimated trapping frequency in the direction of the magnetic-field gradient. After the loading, sites are populated with at most three atoms, which is the upper cutoff of our simulation. Note that $U_1 = 7.40 \times 10^{-2} U_0$, $U_2 = 0.795 U_0$, and $U_3 = -4.71 \times 10^{-3} U_0$. The gradient, which does not vary with lattice depth, is given by $\gamma_B b(\mathbf{r}_i) = 29 \times 10^6$ Hz m^{-1} $\times$ $\mathbf{r}_i \cdot \hat{\mathbf{u}}_Z$, where the lattice spacing in the $\hat{\mathbf{u}}_Z$ direction is 269 nm. The values of the quadratic Zeeman shifts used in the simulations are given in Fig. 3(o).

Parameter (Hz)	$V_0 = 3E_r$	$V_0 = 9E_r$	$V_0 = 15E_r$
U_0/h	1250	2860	4190
$\omega_Z/2\pi$	279	337	387
J_X/h	917	106	18.6
J_Y/h	11.8	5.67×10^{-2}	1.11×10^{-3}
J_Z/h	1380	297	82.3
$U_{dd}(\mathbf{0})/h$	−6.96	−15.9	−23.2
$U_{dd}(\pm\mathbf{u}_X)/h$	2.86	3.02	3.02
$U_{dd}(\pm\mathbf{u}_Y)/h$	−0.176	−0.175	−0.175
$U_{dd}(\pm\mathbf{u}_Z)/h$	−2.52	−2.60	−2.62

$m = -3$ sublevel into the optical lattice at the desired depth V_0. We assume that the atoms are initially in equilibrium.

A fast $\pi/2$ microwave pulse ($\sim$5 μs long) is then applied to rotate the atomic spins to be along the spin x axis, thus in a superposition of all seven Zeeman sublevels. The corresponding populations $N_m(t)$ are then measured as a function of hold time after the pulse, using Stern-Gerlach imaging. The observed evolution in these populations (see data in Fig. 3) motivates the theoretical analysis that we develop in the following section. For our parameters the superfluid to Mott insulator transition is predicted to occur according to the Gutzwiller model at approximately $V_c \approx 8E_r$, where E_r is the recoil energy for $\lambda = 532$ nm.

III. THEORETICAL METHODS

A. Gutzwiller method

The Gutzwiller method is a mean-field technique suited to describing bosons in an optical lattice. This approach has been applied to spin-1 bosons (see, e.g., [28,29]), but here we consider the extension of this method to describe spin-3 bosons with DDIs. The Gutzwiller method treats on-site terms exactly and intersite couplings (due to tunneling and interactions) at the mean-field level. The system state in this method is written as a product of states at each lattice site, i.e.,

$$|\psi(t)\rangle_G = \prod_i |\psi(t)\rangle_i, \tag{5}$$

$$|\psi(t)\rangle_i = \sum_{\mathbf{N}} f^i_{\mathbf{N}}(t)|\mathbf{N}\rangle_i, \tag{6}$$

where $|\mathbf{N}\rangle_i = |N_3, N_2, N_1, N_0, N_{-1}, N_{-2}, N_{-3}\rangle_i$ is the spin-3 Fock state basis at site i and $f^i_{\mathbf{N}}$ are the respective amplitudes of the on-site expansion. It can then be shown that the equation of motion for the state at site i is given by

$$i\hbar\frac{d}{dt}|\psi(t)\rangle_i = \hat{H}^i_G|\psi(t)\rangle_i, \tag{7}$$

where $\hat{H}^i_G$ is the Hamiltonian at lattice site i. This contains the exact on-site Hamiltonian $\hat{H}_i$ with all the on-site terms of Eq. (1) and the mean-field contribution from nearest neighbors, giving [37]

$$\begin{aligned}\hat{H}^i_G = \hat{H}_i &- \sum_\alpha J_\alpha \sum_{j^{(i)}_\alpha}\sum_m \left[\langle \hat{a}_{m,j^{(i)}_\alpha}\rangle\left(\hat{a}^\dagger_{m,i} - \frac{1}{2}\langle \hat{a}^\dagger_{m,i}\rangle\right) + \text{H.c.}\right] \\ &+ \sum_{m,m',n,n'}\sum_{j\neq i} D^{mm'nn'}_{ij}\langle \hat{a}^\dagger_{m',j}\hat{a}_{n',j}\rangle \\ &\times\left(\hat{a}^\dagger_{m,i}\hat{a}_{n,i} - \frac{1}{2}\langle \hat{a}^\dagger_{m,i}\hat{a}_{n,i}\rangle\right),\end{aligned} \tag{8}$$

where $j^{(i)}_\alpha$ are the nearest neighbors to site i in the α direction and we also choose to include only the sum over nearest neighbor j in the DDI term.

The Gutzwiller ansatz reduces the Hilbert space dimension significantly and couples sites only through mean-field terms. As such, if every site is identical, the 3D problem only requires the solution at one site, i.e., $f^i_{\mathbf{N}}(t) \to f_{\mathbf{N}}(t)$ for all i. However, in our problem the magnetic-field gradient and the harmonic confinement break the translational symmetry. Thus, the system can no longer be reduced to a single site within the Gutzwiller approximation. To produce a computationally tractable case we use a model with spatially varying coefficients only along the $\mathbf{u}_Z$ direction and assume the other two perpendicular directions to be spatially invariant, i.e., we use the ansatz $f^{i_Z}_{\mathbf{N}}(t)$ to describe the dynamics which assumes the sites $i = (i_X, i_Y, i_Z)$ behave identically to $(0, 0, i_Z)$. This choice leaves us explicitly modeling an effective one-dimensional problem along the direction of the gradient field, as schematically shown in the inset to Fig. 1, yet allows us to retain the 3D character of the long-range DDIs and tunneling.

Due to the spin degrees of freedom, the local Hilbert space grows rapidly with the number of atoms per site. We restrict $f^{i_Z}_{\mathbf{N}}$ to $\{\mathbf{N} : \sum_m N_m \leqslant 3\}$, i.e., up to three atoms per site, which should be adequate as the experimental initial state typically has some occupation of doublons (i.e., sites with two atoms), but the number of triply occupied sites is negligible both initially and during the dynamics. To match the experimental system we consider a system of 30 lattice i_Z sites (see Appendix A for additional details). The initial state is computed by finding the Gutzwiller ground state for $N_{\text{tot}} = 18$ atoms (occupying the 1D line of sites along the gradient direction), all restricted to the $m = -3$ sublevel. We note that this choice for N_{tot} does not reproduce the initial number of doublons observed experimentally. However, in the experiment the total number of atoms is observed to decrease rapidly with time as $N(t) \approx N(0)\exp(-\gamma t)$, where $\gamma \approx 100\ \text{s}^{-1}$ (see Appendix B) due to dipolar relaxation. Our Gutzwiller theoretical model does not include losses, but our choice of N_{tot} gives a doublon fraction closer to the average value observed experimentally over the $\lesssim$10 ms time period. This accounts for the rapidly decaying population of doubly occupied sites and our effective trapping conditions (the choice of N_{tot} is discussed further in Sec. IV B). The initial-state density distribution for various lattice depths is shown as the black line in Fig. 3(p), with the result for $V_0 = 15E_r$ demonstrating a uniformly filled Mott insulator state. To initiate the dynamics we apply a $\pi/2$ spin rotation about the y axis to this initial state.

B. GDTWA

In the deep lattice regime we describe the system with a spin Hamiltonian of the form

$$\begin{aligned}\hat{H} = &\gamma_B\sum_i b(\mathbf{r}_i)\hat{S}^z_i + q\sum_i\left(\hat{S}^z_i\right)^2 \\ &+ \frac{1}{2}\sum_{i,j\neq i} U_{dd}(\mathbf{r}_i - \mathbf{r}_j)\left[\frac{1}{2}\left(\hat{S}^x_i\hat{S}^x_j + \hat{S}^y_i\hat{S}^y_j\right) - \hat{S}^z_i\hat{S}^z_j\right],\end{aligned} \tag{9}$$

where the first two terms account for the linear and quadratic Zeeman fields and the last term describes the long-range dipolar interactions that couple Cr atoms in different sites. A fraction of sites are doubly occupied in the experiment and we model each of these sites as a pseudoatom of spin 6, i.e., the maximum total spin of two spin-3 Cr atoms, and their dynamics are still governed by Eq. (9), but with $\hat{S}^{x,y,z}$ replaced by operators corresponding to $S = 6$. This treatment is motivated by the fact that the initial spin state

for each doubly occupied site is in the symmetric $S = 6$ manifold and the dominant on-site contact interactions do not change this total spin [see Eq. (2)]. We have also checked numerically that this is a good approximation. We solve the spin dynamics under the Hamiltonian (9) by applying the GDTWA, a numerical approach first introduced in Ref. [15]. In the GDTWA approach, quantum dynamics is obtained by properly sampling the initial quantum state in phase space and averaging over the ensuing trajectories [38]. The GDTWA method has been shown to be capable of capturing quantum correlations developed during spin dynamics [15,27]. With this method, we are able to perform calculations including the effect of quantum fluctuations in a relatively large system (lattice size $13 \times 6 \times 13$) and check that a convergence in system size is reached within experimental uncertainties. The population of a spin state m is obtained via combining the contributions from both singly and doubly occupied sites

$$N_m(t) = \eta(t) \sum_{M=-6}^{6} \langle 3, m, 3, M-m|6, M\rangle^2 N_M^{S=6}(t) + [1-\eta(t)] N_m^{S=3}(t), \tag{10}$$

where $N_M^{S=3,6}(t)$ is the averaged population on a spin state M calculated for the singly and doubly occupied sites, respectively. The term $\langle 3, m, 3, m'|6, M\rangle$ denotes the Clebsch-Gordan coefficients and η denotes the fraction of atoms in doubly occupied sites. Due to atom loss from doubly occupied sites, η varies with time. The time dependence that we use for η is extracted from experimental measurements of the total atom number $N(t)$ (see Appendix B).

C. Perturbative treatment

Due to the complexity of the Hamiltonian (1), many factors play a role in the system evolution following the spin rotation. In order to have a better grasp of the contributions of the various terms in the Hamiltonian, we first consider the dynamics of the system in the short-time limit using perturbation theory.

We consider the dynamics of an initial state with $N = 2$ atoms occupying two neighboring lattice sites, $i = 1, 2$, described by the initial state

$$|\psi(0)\rangle = \sum_{m,n=-3}^{3} f_m f_n \hat{a}_{m,1}^\dagger \hat{a}_{n,2}^\dagger |0\rangle_1 |0\rangle_2.$$

where $|0\rangle_i$ is the vacuum state in site i. The f_m coefficients specify the different spin amplitudes after the spin rotation, $f_0 = -\frac{\sqrt{5}}{4}$, $f_{\pm 1} = \frac{\sqrt{15}}{8}$, $f_{\pm 2} = -\sqrt{\frac{3}{32}}$, and $f_{\pm 3} = \frac{1}{8}$. To second order in t the evolution of the population of the different Zeeman levels is given by

$$N_m^{(2)}(t) = \langle \hat{N}_m(0)\rangle - it\langle[\hat{N}_m, \hat{H}_2]\rangle - \frac{t^2}{2}\langle[[\hat{N}_m, \hat{H}_2], \hat{H}_2]\rangle, \tag{11}$$

where $\hat{H}_2$ is the Hamiltonian (1) specialized to two sites separated by $\mathbf{u}_Z$.

We find that the term proportional to t vanishes, and to second-order in t, the spin population dynamics for $m = 0$ is given by

$$N_0^{(2)}(t) = \tfrac{5}{8} - \tfrac{45}{16} t^2 U_{dd}(\mathbf{u}_Z)\big[q + \tfrac{3}{4} U_{dd}(\mathbf{u}_Z)\big]. \tag{12}$$

The evolution of the population of the other sublevels is of a similar form and presented in Appendix C. We have also ignored in the perturbative treatment the dynamics of doubly occupied sites. As explained in Appendix C 3, the perturbative treatment tends to break down very quickly when those terms are included and a better approximation is obtained when they are excluded. We also note that up to this order, our perturbative result immediately generalizes to the many-body system by simply summing over all pairs of particles.

Equation (12) provides valuable insight into the short-time dynamics of the system. First, it shows that the DDIs between neighboring sites and the quadratic Zeeman term are what drive the dynamics at short times for all lattice depths. Tunneling or linear magnetic-field gradients, when present, only cause redistribution of the spin populations at a higher order (see Appendix C 2).

IV. ANALYSIS OF DYNAMICS

A. Double-well dynamics

The computational complexity of simulating the Hamiltonian (1) makes any exact treatment beyond a few lattice sites challenging. In order to benchmark our methods we compare the predictions of the Gutzwiller dynamics and the perturbative expressions obtained above to the exact dynamics of a double-well system with two atoms. In Fig. 2(a) we plot the proportion of doubly occupied sites (doublons) in the initial states. This shows that the Gutzwiller approximation predicts that the sites become singly occupied for $V_0 \gtrsim 8E_r$, indicating the existence of a superfluid to Mott insulator transition at $V_0 \approx 8E_r$ (we adjusted the tunneling and nearest-neighbor DDIs so the lattice depth at which the transition occurs is similar to the 3D system). In contrast, the exact double-well result shows that the doublon fraction varies smoothly with lattice depth. Nevertheless, the range of lattice depths where doubly occupied sites are dominant is well captured by the Gutzwiller model. Figures 2(b)–2(f) compare the perturbative, exact, and Gutzwiller dynamics for the $m = 0$ population. As a mean-field method the Gutzwiller approach is not expected to provide an accurate description of a two-particle system; however, the comparison reveals that Gutzwiller results are qualitatively correct for low lattice depths $V_0 \lesssim 8E_r$. In this regime the populations tend to oscillate. Furthermore, we note that we have not included the role of doubly occupied sites in the above expressions (see Appendix C for the full results). We find that by including the doublon sites the solution matches the initial curvature of the exact solution [see the inset of Fig. 2(b)]. However, this leads to a divergence between the two approaches for longer times (see Appendix C 3). The slower dynamics of the second-order perturbation theory for singly occupied sites follows the exact solution for a longer time as shown throughout the figures. For deeper lattices $V_0 > 9E_r$, where the system is in the insulating regime and doublons are negligible, the N_0 population tends to decay and is well described by the perturbative result. In this regime, in contrast, the Gutzwiller model shows suppressed population dynamics. This reveals the failure of the method to account for the necessary quantum fluctuations that mainly drive the dynamics in the frozen-atom limit.

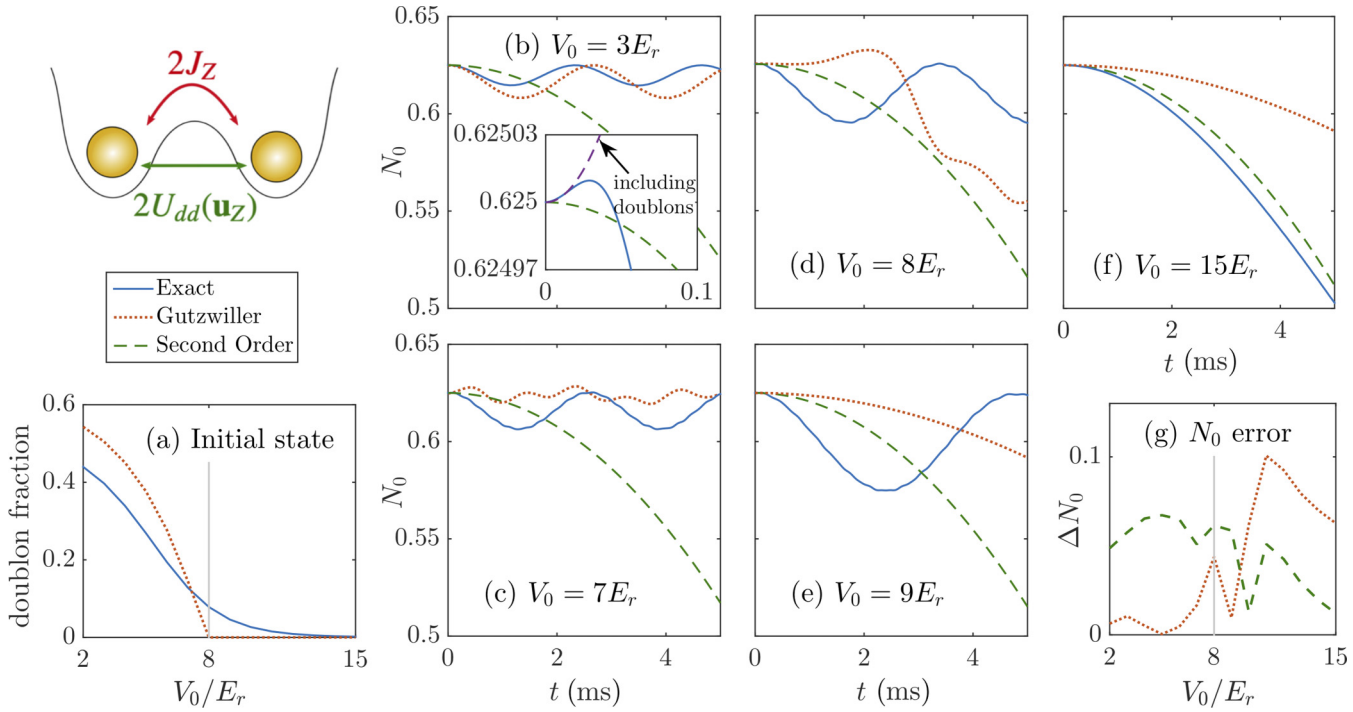

FIG. 2. Comparison of predictions for N_0 population dynamics in the double-well system $\hat{H}_2$. (a) Doublon fraction of the two-particle initial state. (b)–(f) The population of the $m = 0$ substate as a function of time for a double-well system allows us to compare the short-time perturbative expansions at second-order to the Gutzwiller dynamics, as well as the exact dynamics for five different lattice depths. In the deep lattice the second-order formula is a good approximation for longer times. The simulations parameters are given in Table I, with the tunneling and nearest-neighbor DDIs adjusted so the lattice depth at which the transition occurs is similar to the 3D system and $q/h = 2$ Hz. The inset in (b) shows the perturbative result (12) extended to include doublons, demonstrating that they give rise to rapid short-time dynamics captured in the exact solution, but limiting the applicability of the perturbative result to short times. (g) Difference of Gutzwiller and second-order populations compared to the exact population at 4 ms, as a function of lattice depth.

To quantify the validity of the different methods, in Fig. 2(g) we plot the accumulated error during the time evolution vs lattice depth. It explicitly shows that while the Gutzwiller model gives a better description at low lattice depths, the perturbative formula describes well the short-time dynamics in the Mott regime. Note that the GDTWA results were not shown in this two-site comparison as the GDTWA is a method based on semiclassical trajectories, and thus requires $N \gg 2$ for convergence.

B. Full system dynamics

In this section we use the Gutzwiller ansatz and the GDTWA to study the dynamics of larger systems in the parameter regimes used for the experimental measurements of the spin population dynamics. As discussed above, in the Gutzwiller model we do not include the particle loss (due to dipolar relaxation) dynamically. Instead, we account for it by sweeping over a range of particle numbers N_{tot} and find that the experimental dynamics is best captured by $N_{\text{tot}} = 18$. We note that the Gutzwiller treatment is not adequate in the deep lattice limit, where we use the GDTWA formalism, including the doublons and losses, to account for the observed dynamics.

The second fitting parameter of the theory is the quadratic Zeeman shift q. Since it arises from tensorial light shifts, it is expected to vary with lattice depth V_0, and while its precise value is not known *ab initio*, experimental evidence [15] suggests that its magnitude is bounded by $|q/h| \leqslant 6$ Hz in the range of lattice depths considered. The observed dynamics, most notably at short times, depends strongly on the sign and magnitude of q [see, e.g., Eq. (12)]. We have determined the values of q that give the best fit to the initial dynamics. The optimized values of q are shown in Fig. 3(o) for the Gutzwiller and GDTWA methods.

For $V_0 < 10E_r$ the optimal value of q determined from the Gutzwiller method is within the expected range of values. However, for deeper lattices a much larger q value is required to achieve dynamics of magnitude similar to that observed experimentally. This suggests that the Gutzwiller dynamics is failing in the deep lattice regime, consistent with our observations of the double-well dynamics. In fact, we know that quantum fluctuations, which play a key role in driving the dynamics in the Mott insulator regime, are not accounted for in the Gutzwiller model. Hence, the artificially large q value obtained when fitting Gutzwiller results to the experimental data compensates for the absence of these fluctuations in the simulation. For the GDTWA calculations a value of $q/h = 2$ Hz is found to provide good agreement for all lattice depths greater than $8E_r$.

In Fig. 3(p) we show the spatial distributions of the different levels at $t = 5$ ms and various lattice depths in the Gutzwiller model, which is a feature that has not been resolved in our experiment. At low lattice depths (see the

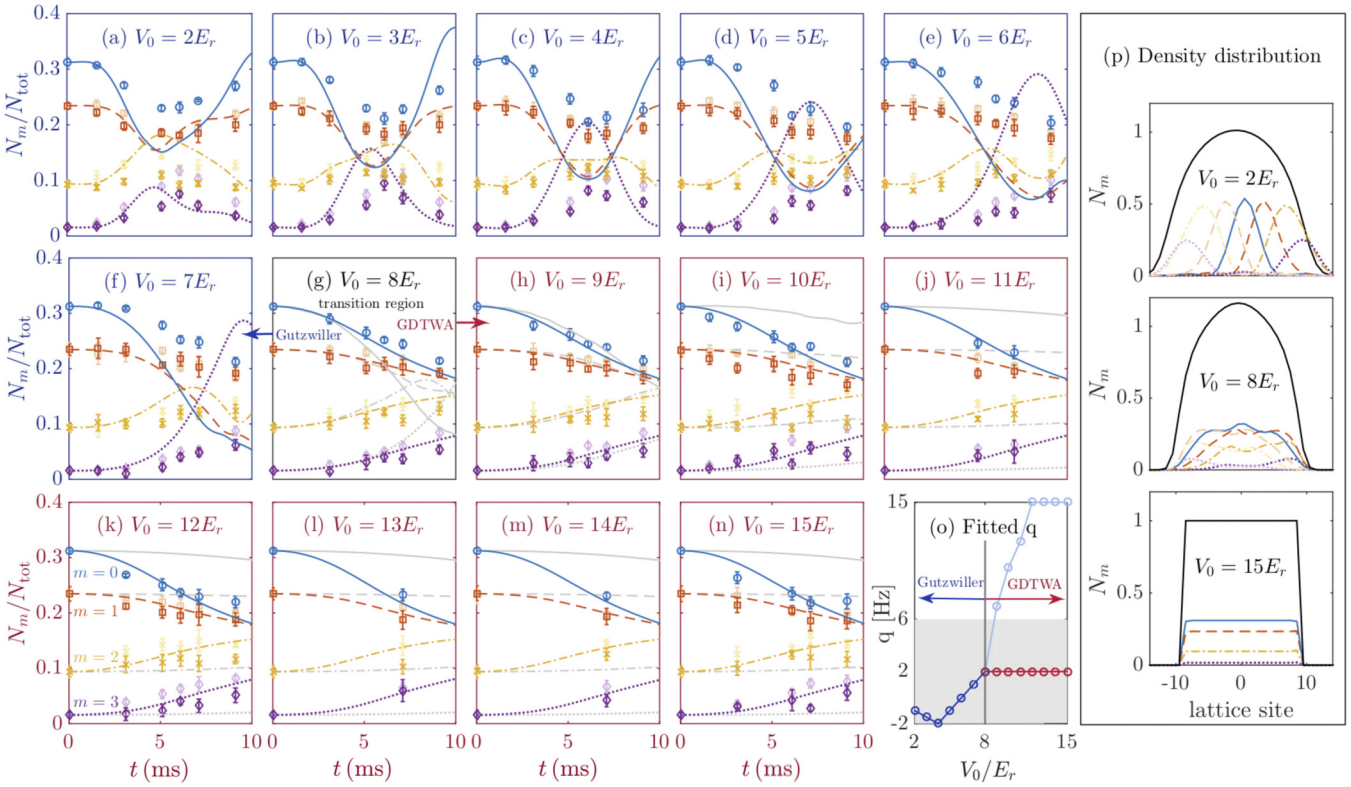

FIG. 3. Comparison of simulation (lines) to experiment (markers). Blue (solid line with circles) indicates $m = 0$, red (dashed line with squares) indicates $m = 1$, yellow (dot-dashed line with crosses) indicates $m = 2$, and purple (dotted line with diamonds) indicates $m = 3$. Pale markers indicate the negative m experimental populations. For $V_0 < V_c$ the Gutzwiller model is shown, while for $V_0 \geqslant V_c$ the GDTWA model is shown, with the corresponding $q/h = 2$ Hz Gutzwiller solution shown in gray. Experimental error bars are from statistical standard errors and from 10% uncertainty in the estimated lattice depths. (o) Quadratic Zeeman field q fitted at each lattice depth in the simulations based on the Gutzwiller ansatz and the $q/h = 2$ Hz value used in the GDTWA. The light gray region indicates the range of acceptable q values. The light blue circles correspond to optimal values for the Gutzwiller approximation which however are outside the acceptable range. (p) Distribution of the whole cloud across the lattice at $t = 0$ (black line) and distribution of individual Zeeman levels across the lattice at $t = 5$ ms.

$V_0 = 2E_r$ result) the Gutzwiller method shows that the spin states spatially separate in wave packets that are appreciably narrower than the initial density distribution (black). The spin-dependent transport is driven by the magnetic-field gradient and causes the center of mass of the various wave packets to undergo spatial oscillations. The packets tend to be well separated at the time when there is a large dip in the N_0 population in Fig. 3(a) (and corresponding peak in the higher $|m|$ populations). This observation emphasizes the relevant role played by the interplay between the magnetic-field gradient, which drives the spin transport, and the spin-dependent contact interactions which lead to a redistribution of the spin populations as observed in the Gutzwiller predictions [see Figs. 3(a)–3(d)]. As the lattice depth increases spin transport is inhibited and the wave-packet oscillations gradually become less visible. The Gutzwiller results for the density distributions at $V_0 = 8E_r$ reveal a small center-of-mass separation of the spin components (here the wave packets are broad and mostly overlapping). The Gutzwiller solution predicts that the system will become fully insulating, with one atom per site and all transport dynamics freezing out, as the lattice depth exceeds a critical value of $V_c \approx 8E_r$. For $V_0 > V_c$ the Gutzwiller model fails to capture the experimentally observed spin population dynamics. In contrast, in this regime the GDTWA is able to reproduce very well the observed dynamics, even for V_0 as shallow as V_c, as shown in Figs. 3(h)–3(n).

The sharp change of behavior of the Gutzwiller dynamics as the system crosses the Mott insulator transition is further illustrated in Figs. 4(a)–4(c), which show the $m = 0$ populations with lattice depth at three times. There we can observe that the Gutzwiller calculations show almost no dependence as a function of lattice depth as soon as the Mott transition is reached. This can also be seen in Fig. 3, which shows that dynamics almost disappears in the Gutzwiller approach above V_c. Such a change in behavior around $V_c = 8E_r$ is also observable in the experimental result but in a much less pronounced way. This is because, above the Mott transition, spin dynamics mainly occurs due to intersite DDIs and involves the growth of quantum correlations, a feature which can be reproduced by the GDTWA approach [15] but not by the Gutzwiller simulations. As a consequence, there still exists significant dynamics at large lattice depths, which the Gutzwiller ansatz fails to capture.

Although we only observe a gradual and smooth evolution of spin dynamics as the lattice spans the Mott to superfluid

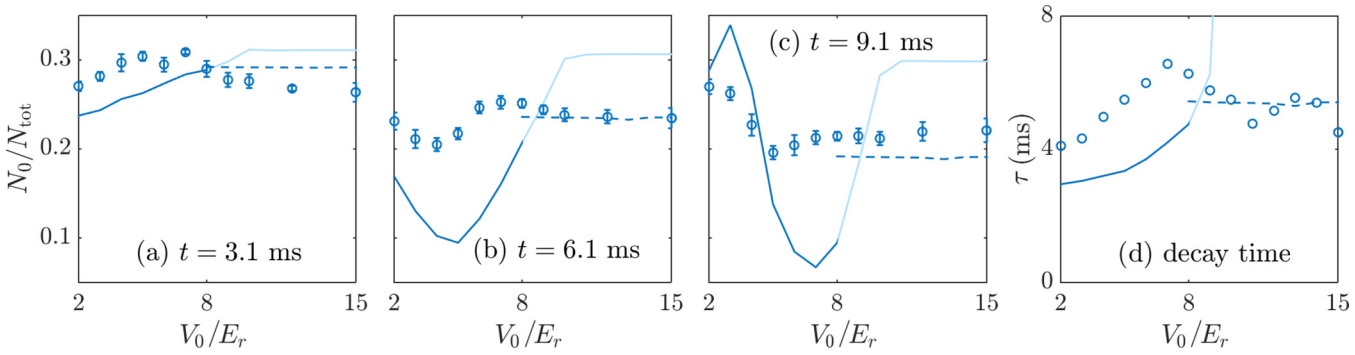

FIG. 4. (a)–(c) Gutzwiller (solid line) and GDTWA (dashed line) $m = 0$ populations compared to experimental results (symbols) as a function of lattice depth. (d) Time τ for $m = 0$ population to decay to $N_0/N_{\rm tot} = 0.25$.

transition, it is worth pointing out that the observations are qualitatively different above and below the transition. Below the transition an oscillation is observed and above the transition the population follows a monotonic evolution, with a weak lattice depth dependence. To better quantify this claim, we plot in Fig. 4(d) the time at which the $m = 0$ fractional populations decay from their initial value to 0.25. A clear difference is observed below and above the Mott transition. While the Gutzwiller model overestimates the amplitude of the oscillation for $V_0 < V_c$, it correctly captures its shape. In particular, it is able to capture the slowing down of the dynamics which is experimentally observed as the lattice depth is raised, as highlighted in Fig. 4(d). To physically understand this slowing down, it is worth referring to our recent results [30], which show that when the dipoles are tilted compared to the magnetic-field axis by $\pi/2$, no spin dynamics can arise in the absence of magnetic-field gradients. The point is that for Cr atoms the dominant component of the contact interactions (set by the c_1 coefficient; see Appendix B) tends to favor alignment and prevent demagnetization. To leave the initially polarized stationary state, a coupling between spin and motional degrees of freedom is needed, which is here provided by the gradient of the magnetic field. As shown in Fig. 3(p), an important effect of the lattice potential is to reduce the relative motion of the different spin states, therefore reducing the effect of the magnetic-field gradient and also effectively screening the role of contact interactions in the population dynamics by favoring sites populated by a single atom. Under these conditions, DDIs become dominant. The interplay of DDIs with magnetic-field gradients and quadratic shifts all together can cause spin demagnetization. For the range of lattice depths accessible in the experiment the time decay rate is almost independent of lattice intensity, as shown in Fig. 4(d).

The GDTWA successfully captures the magnitude of the population decay for $V_0 > V_c$. In fact, an unexpected outcome of the comparison between the experimental data and the GDTWA is that GDTWA reproduces well the dynamics even for lattice depths barely above the Mott transition. At large lattice depths, the disagreement of the experimental data with Gutzwiller results together with the good agreement with the GDTWA approach confirms that a new regime is reached where the spin dynamics is governed by different physical processes. As mentioned above, the large lattice depth regime is impacted by strong quantum correlations. We also observe in the simulations that while spin dynamics is mostly driven by contact interactions at shallow lattice depths, it is almost entirely driven by DDIs at large lattice depths ($V_0 > V_c$).

V. TOTAL MAGNETIZATION AND GAP PROTECTION

The dynamical evolution of the populations of the Zeeman levels, as presented in Figs. 3(a)–3(n), varies smoothly when crossing the underlying superfluid to Mott insulator transition. In order to better understand the spin dynamics in both the superfluid and Mott insulator regimes, we now study the dynamics of the collective spin length, corresponding to the total magnetization, which we find better reveals the underlying abrupt transition. It is given by

$$\langle \bar{S} \rangle = \sqrt{\langle \hat{S}^x \rangle^2 + \langle \hat{S}^y \rangle^2 + \langle \hat{S}^z \rangle^2}. \tag{13}$$

Here $\hat{S}^{x,y,z} = \sum_i \sum_{m,n} S^{\alpha}_{mn} \hat{a}^{\dagger}_{m,i} \hat{a}_{n,i}$ are collective spin observables. For the case of an initial state following a $\pi/2$ rotation, the quantity $\langle \hat{S}^z \rangle$, which is conserved during the dynamics, is equal to zero, and therefore $\langle \bar{S} \rangle = \sqrt{\langle \hat{S}^x \rangle^2 + \langle \hat{S}^y \rangle^2}$.

In Fig. 5 we plot the dynamics of the collective spin length obtained by the Gutzwiller predictions ($V_0 < 8E_r$) and GDTWA ($V_0 \geqslant 8E_r$). The dashed green line also shows the short-time dynamics obtained from perturbation theory of the double-well system up to terms quadratic in time, $O(t^2)$, summed over pairs of atoms at neighboring lattice sites:

$$\langle \bar{S} \rangle \sim \sum_i N^i \Bigg(3 - \frac{3t^2}{2} \Bigg[5q^2 + [\gamma b(\mathbf{r}_i)]^2 + \frac{27}{2} \sum_{j^{(i)}} [U_{dd}(\mathbf{r}_i - \mathbf{r}_j)]^2 \Bigg] \Bigg), \tag{14}$$

where N^i is the population at site i and the sum over $j^{(i)}$ includes all of site i's nearest neighbors. This is dominated by the large magnetic gradient term and is therefore largely independent of lattice depth.

The collective spin length provides direct information of the spin coherence and it is experimentally accessible in a Ramsey sequence [8,9,30] performed by applying a $\pi/2$ pulse after the free evolution before measuring the population. Measurements of the collective spin length can also be obtained from Faraday rotation spectroscopy as this technique gives

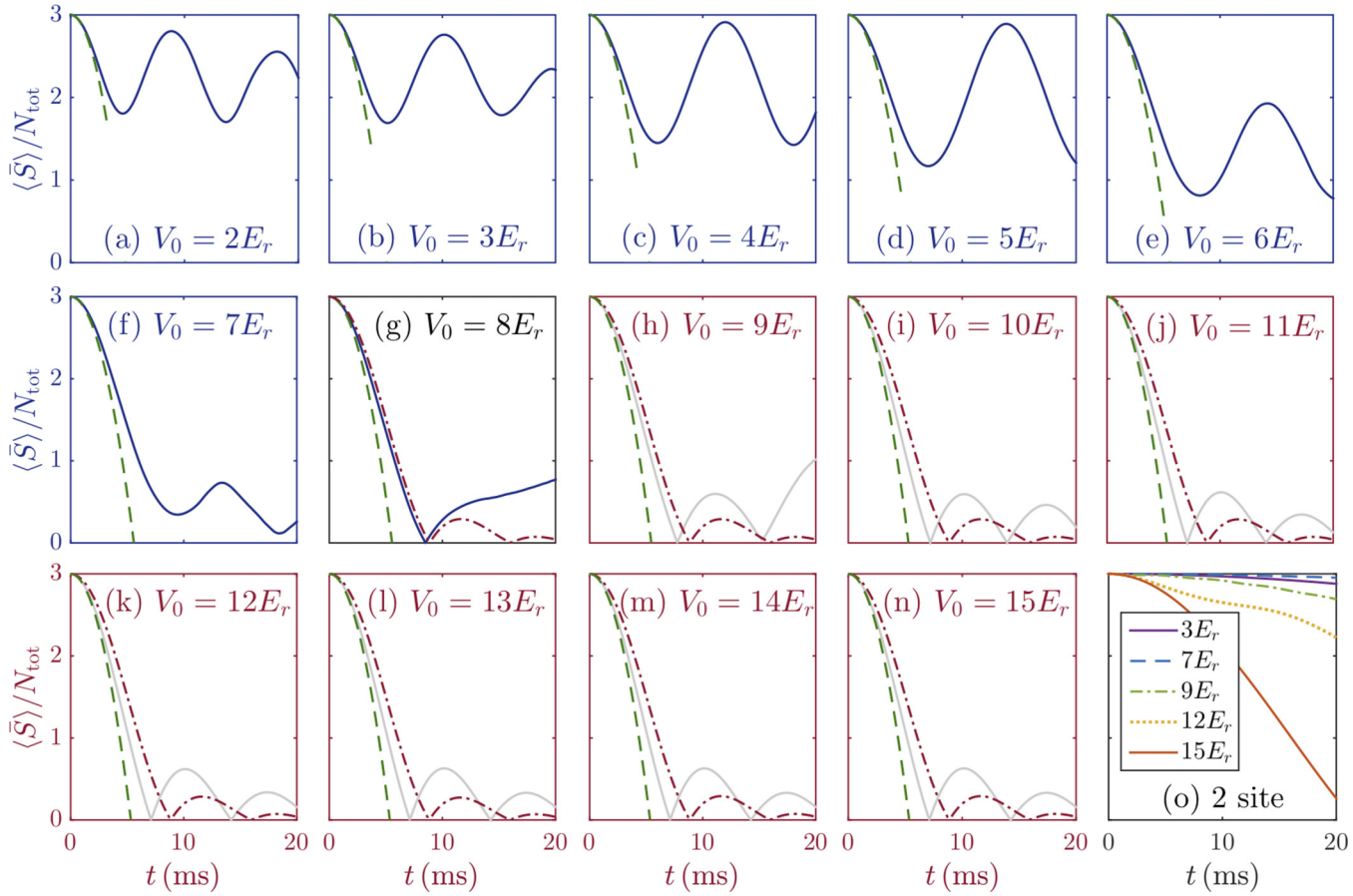

FIG. 5. Total spin as defined by Eq. (13) for a range of lattice depths. The blue solid line indicates the total spin using the Gutzwiller model, with the results beyond the lattice depth V_c that the Gutzwiller model is considered reliable shown in gray. The red dot-dashed line indicates the GDTWA result and the green dashed line gives the short-time second-order expansion, found by summing Eq. (14) over all pairs of atoms. (o) Total spin in a double-well system (see Fig. 2) using the exact method with different lattice depths.

access to the transverse spin component [39–41]. Two leading processes are expected to generate magnetization decay: the field gradient and the interactions. While the magnetic gradient generates single-particle dephasing since it causes different lattice sites to precess at slightly different rates, interactions entangle the spins leading to a loss of information when one traces out over a part of the total system as one does when computing local observables such $\langle \hat{s}_i^{x,y} \rangle$ (see, e.g., Ref. [15]). The quadratic Zeeman term can also lead to magnetization decay in this case due to the development of intraspin correlations, i.e., correlations between the individual electrons inside each atom [42].

While generically interactions and inhomogeneities both can lead to magnetization decay, the spin-dependent interactions proportional to U_1 in Eq. (2) counterintuitively can favor spin alignment for weakly interacting atoms. This is because these interactions open a gap in the energy spectra that can suppress dephasing processes as experimentally demonstrated in recent work [22,30,43]. Signatures of the gap protection can be observed in Gutzwiller predictions for shallow lattices [Figs. 5(a)–5(f)]. The protection is present when there is more than one atom per lattice site and when the U_1 term can lock the spins favoring alignment. This manifests as an oscillatory behavior in the collective spin length instead of rapid decay. The protection however enters as a higher-order process and it is not observable in the perturbative analysis that neglects third- and higher-order terms in time. The perturbative analysis however does provide a relatively good description of the short-time dynamics.

In the Mott regime, on the other hand, interactions and magnetic-field gradient cooperate and both lead to a fast decay of the contrast as can be observed in the GDTWA simulations [Figs. 5(h)–5(n)]. Similar behavior is observed in the exact solution of a double-well system [Fig. 5(o)], validating the behavior observed in the many-body system.

The relatively sharp transition between oscillatory and overdamped behavior around the critical point ($V_0 = 7E_r$ to $V_0 = 8E_r$) might be overestimated in the Gutzwiller approximation but might survive in the full quantum system. Experimental measurements of the contrast will be needed to test if this is the case.

VI. CONCLUSION

In this work we have presented extensive theoretical and experimental comparisons of the dynamics of itinerant spin-3 Cr atoms in a 3D optical lattice and subject to harmonic trapping along all three directions. The microscopic Hamiltonian governing the dynamics of the system is complex and features single-particle motion, as well as contact, and long-range

dipolar interactions. Exact modeling of the experimental dynamics exceeds the capabilities of classical computation, so to compare to our experimental results we have developed a variety of approximate models. First, we studied the exact population dynamics of the Zeeman levels of a two-site system and compared our results to a Gutzwiller treatment, as well as a short-time perturbative treatment. We thus demonstrated that for shallow lattice depths below the superfluid to insulator phase transition at V_c, where a significant portion of the sites are doubly occupied, the Gutzwiller description provides a good qualitative description of the exact dynamics. However, we found that the Gutzwiller description fails to reproduce the exact dynamics for large lattice depths, above the Mott transition. For large lattice depths, on the other hand, we have used an effective spin model description (GDTWA) whose short-time dynamics was shown in [15] to match the exact solution for large enough lattice depths, where tunneling and double occupancy are suppressed.

Armed with the above intuition, we applied the Gutzwiller approximation to lattice depths $V_0 < V_c$ and the GDTWA method, which incorporates the effect of quantum fluctuations, to $V_0 > V_c$ to benchmark the experimental observations. We observed qualitative agreement between the experimental results and the theoretical studies, which confirms that these approximate methods can be trusted in their respective domain of validity. In turn, the comparison with these two models provides unique physical insights regarding the physics at play for different lattice depths. While for lattice depths $V_0 > V_c$ dipolar interactions and quantum effects play an essential role in the observed dynamics, we found that for $V_0 < V_c$ transport and contact interactions both play an essential role (while intersite quantum correlations can then be neglected). Our analysis thus shows that the two different regimes of low and high lattice depths are qualitatively different. This can indeed be seen by contrasting the behavior of spin dynamics in these two regimes: While the spin dynamics is oscillatory and lattice depth dependent for $V_0 < V_c$, the behavior is mostly monotonic and lattice depth independent for $V_0 > V_c$. The crossover between these two behaviors is however smooth and does not reveal the sharp underlying Mott insulator to superfluid transition. Therefore, we propose an experimental measurement of the spin length which can be readily implemented experimentally, as it should display a more pronounced change in behavior as the system crosses from the superfluid to the Mott insulator regime.

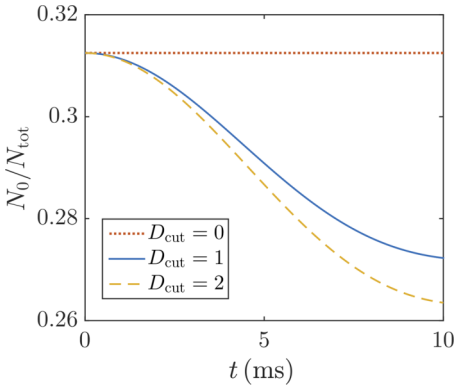

FIG. 6. Comparison of DDI cutoff approximations in the Gutzwiller model for $V_0 = 15E_r$ and $q/h = 15$ Hz. When $D_{\rm cut} = 0$ only on-site DDIs are included, when $D_{\rm cut} = 1$ nearest neighbors (including diagonal nearest neighbors) are included, and when $D_{\rm cut} = 2$ next-nearest neighbors are also included. We see that the contribution from next-nearest neighbors is small compared to the nearest neighbors. As intersite DDIs are most important in the deep lattice limit, this conclusion will hold for all lattice depths.

ACKNOWLEDGMENTS

We thank Johannes Schachenmayer for useful discussions and Asier Pineiro and Andrew Wilson for reviewing the manuscript. A.M.R was supported by the Air Force Office of Scientific Research (AFOSR) Grant No. FA9550-18-1-0319 and its Multidisciplinary University Research Initiative (MURI), the Defense Advanced Research Projects Agency (DARPA) and Army Research Office (ARO) Grant No. W911NF-16-1-0576, the DARPA DRINQs grant, the ARO single investigator Award No. W911NF-19-1-0210, the National Science Foundation (NSF) Grant No. PHY1820885, the NSF JILA-PFC Grant No. PHY-1734006, and NIST. L.G., S.L., L.V., and B.L.-T. acknowledge financial support from Conseil Régional d'Ile-de-France under DIM Nano-K/IFRAF, CNRS, Ministère de l'Enseignement Supérieur et de la Recherche within CPER Contract, Université Sorbonne Paris Cité, and the Indo-French Centre for the Promotion of Advanced Research - CEFIPRA under Contract No. LORIC5404-1. A.S.-N. was supported by the Australian Research Council Centre of Excellence for Engineered Quantum Systems (Project No. CE170100009) and funded by the Australian Government. B.Z. was supported by the NSF through a grant to ITAMP.

APPENDIX A: NUMERICAL METHODS

The Gutzwiller dynamical equations can be obtained by variationally minimizing $\langle\psi_G|i\hbar\frac{\partial}{\partial t} - \hat{H}|\psi_G\rangle$. This yields a set of nonlinear differential equations for the evolution of the Gutzwiller coefficients $\{f^i_{\mathbf{N}}\}$, i.e.,

$$i\hbar\frac{\partial f^j_{\mathbf{N}}}{\partial t} = F^j_{\mathbf{N}}(\{f^i_{\mathbf{N}}\}), \tag{A1}$$

where $F^j_{\mathbf{N}}(\{f^i_{\mathbf{N}}\}) =_j \langle\mathbf{N}|\hat{H}^j_G|\psi_G(t)\rangle$. The form of the $F^j_{\mathbf{N}}(\{f^i_{\mathbf{N}}\})$ is analytically cumbersome (see, e.g., [44] for the spin-1 case), but is easily evaluated numerically by taking expectations of the various operators terms appearing in $\hat{H}^j_G$ in terms of the Gutzwiller coefficients. From the initial condition, the system of equations (A1) is evolved using an adaptive step Runge-Kutta method, with the tolerance set sufficiently low that the solution converges.

APPENDIX B: PARAMETERS

The coefficients for the contact terms are given by Ref. [35] as

$$\tilde{c}_0 = c_0 - \frac{c_3}{7}, \quad \tilde{c}_1 = c_1 - \frac{5c_3}{84},$$
$$\tilde{c}_2 = c_2 - \frac{5c_3}{3}, \quad \tilde{c}_3 = \frac{c_3}{126}, \tag{B1}$$

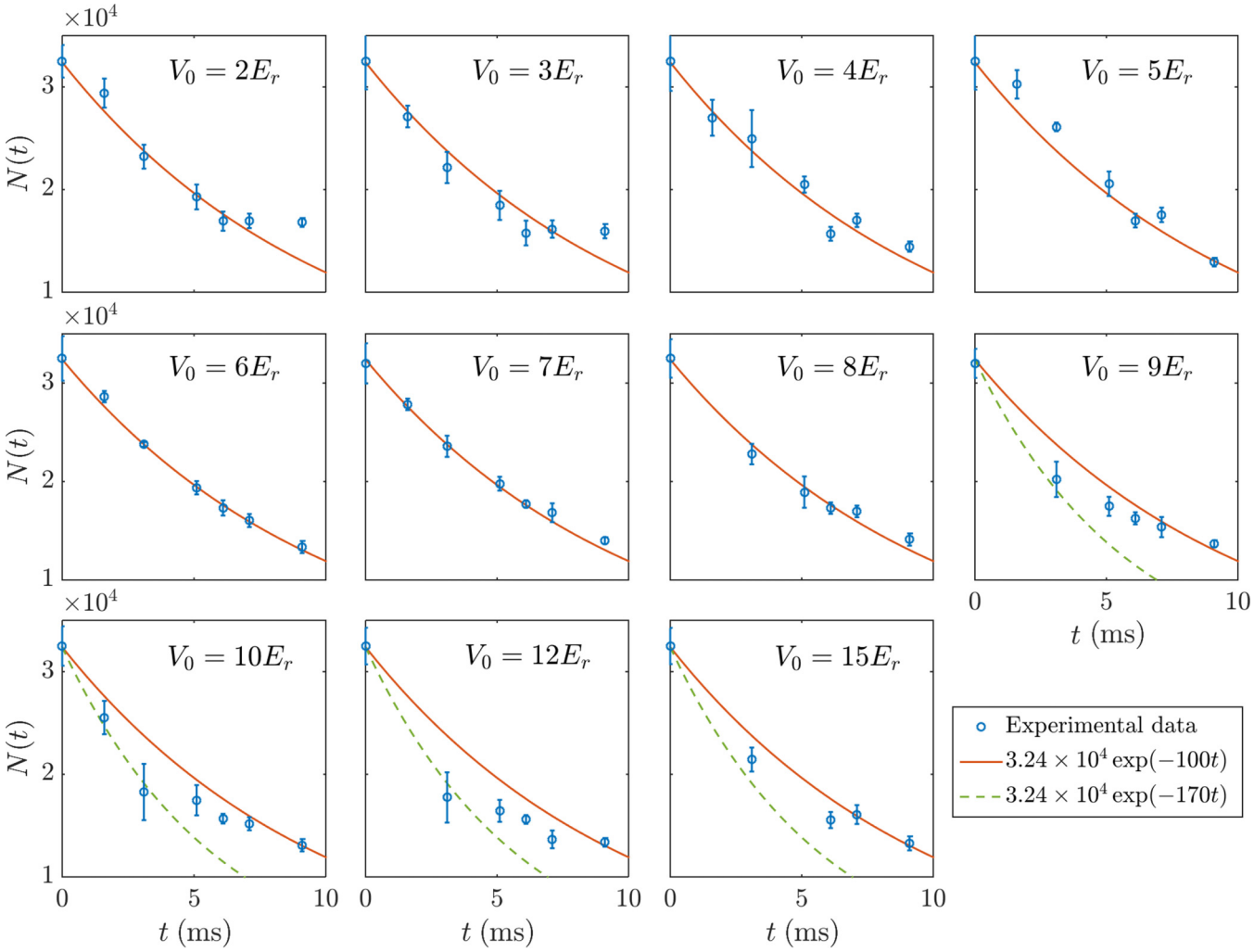

FIG. 7. Experimental values for the total number of atoms in the lattice, along side approximate exponential decay with $\gamma = 100$ and 170 s^{-1}.

where $c_0 = 71 g_c a_B$, $c_1 = 3 g_c a_B$, $c_2 = -15 g_c a_B$, and $c_3 = -46 g_c a_B$ with $g_c = 4\pi\hbar^2/M$ and a_B is the Bohr radius. This gives $U_n = \tilde{c}_n \int d\mathbf{r} |W(\mathbf{r})|^4$. The contact interaction also contains U_2 and U_3 terms

$$C^{mm'nn'} = U_0 \delta_{m,n} \delta_{m',n'} + U_1 \sum_{\alpha} S^{\alpha}_{mn} S^{\alpha}_{m'n'} + \frac{U_2}{7} (-1)^{m+n} \delta_{m,-m'} \delta_{n',-n} + \frac{U_3}{2} \left[\sum_{\alpha\beta} (S^{\alpha} S^{\beta})_{mn} (S^{\alpha} S^{\beta} + S^{\beta} S^{\alpha})_{m'n'} \right], \quad \text{(B2)}$$

which are included in our model but have negligible effect for the states accessible during the dynamics in consideration compared to the larger U_0 and U_1 contributions.

In this paper, with the exception of the GDTWA treatment, we use the nearest neighbor as the cutoff for the dipolar interactions. This is justified, as in shallower lattices where doubly occupied sites exist, the on-site dipolar interactions are dominant. Generally, we find that for the range of lattice depths considered in this paper, the effect of next-nearest-neighbor interactions is small compared to that of nearest-neighbor interactions. We provide a comparison between these terms in Fig. 6.

Atom loss is significant in the experiment, and in Fig. 7 we show the experimental result for the population over time, along with the $N(t) = N(0)\exp(-\gamma t)$ approximation for two values of γ. At low lattice depths $\gamma = 100$ s^{-1} fits the experimental data well, while at larger lattice depths there is an initial fast decay of $\gamma = 170$ s^{-1}, which then slows and returns to the $\gamma = 100$ s^{-1} value by 10 ms.

APPENDIX C: PERTURBATIVE EXPRESSIONS FOR SUBSTATE POPULATION DYNAMICS

1. Short-time dynamics at $O(t^2)$

In the main text, Eq. (12) provides a representative expression for the perturbative (short-time) dynamics of the substate populations for an initial state of singlons. Here we provide the rest of the expressions which take a form similar to those presented in the main text. More generally, we can

write

$$|\psi(0)\rangle = \sum_{m,n} f_m f_n \Big[p_1 \hat{a}^\dagger_{m,1}\hat{a}^\dagger_{n,2} + \frac{p_2}{2}\sqrt{1+\delta_{m,n}}(\hat{a}^\dagger_{m,1}\hat{a}^\dagger_{n,1} + \hat{a}^\dagger_{m,2}\hat{a}^\dagger_{n,2})\Big]|0\rangle_1|0\rangle_2, \tag{C1}$$

where p_1 is the amplitude for the state with one atom per site and $p_2 = \sqrt{1-p_1^2}$ is the amplitude of the state with two atoms on one site and zero on the other, both of which are chosen to be real. To second order in t we find the substate population dynamics is given by

$$N^{(2)}_m(t) = p_1^2 N^{(2)}_{m,\{1,1\}}(t) + p_2^2 N^{(2)}_{m,\{2,0\}}(t), \tag{C2}$$

where we have used $N^{(2)}_{m,\{1,1\}}$ and $N^{(2)}_{m,\{2,0\}}$ to indicate the expectation value of $\hat{N}_m$ for pairs of sites with singlons (n_s) and the number of atoms in a doublon (n_d) configuration, respectively. These are given by

$$N^{(2)}_{0,\{1,1\}}(t) = \frac{5}{8} - \frac{n_s(n_s-1)}{2}\frac{45}{16}t^2 U^1_{dd}\Big(q+\frac{3}{4}U^1_{dd}\Big), \tag{C3}$$

$$N^{(2)}_{0,\{2,0\}}(t) = \frac{5}{8} - \frac{n_d(n_d-1)}{2}\frac{45}{8}t^2 \times \Big(U_1+\frac{1}{2}U^0_{dd}\Big)\Big(q+\frac{3}{4}U^0_{dd}\Big), \tag{C4}$$

$$N^{(2)}_{\pm1,\{1,1\}}(t) = \frac{15}{32} - \frac{n_s(n_s-1)}{2}\frac{45}{64}t^2 U^1_{dd}\Big(q+\frac{3}{4}U^1_{dd}\Big), \tag{C5}$$

$$N^{(2)}_{\pm1,\{2,0\}}(t) = \frac{15}{32} - \frac{n_d(n_d-1)}{2}\frac{45}{32}t^2 \times \Big(U_1+\frac{1}{2}U^0_{dd}\Big)\Big(q+\frac{3}{4}U^0_{dd}\Big), \tag{C6}$$

$$N^{(2)}_{\pm2,\{1,1\}}(t) = \frac{3}{16} + \frac{n_s(n_s-1)}{2}\frac{45}{32}t^2 U^1_{dd}\Big(q+\frac{3}{4}U^1_{dd}\Big), \tag{C7}$$

$$N^{(2)}_{\pm2,\{2,0\}}(t) = \frac{3}{16} + \frac{n_d(n_d-1)}{2}\frac{45}{16}t^2 \times \Big(U_1+\frac{1}{2}U^0_{dd}\Big)\Big(q+\frac{3}{4}U^0_{dd}\Big), \tag{C8}$$

$$N^{(2)}_{\pm3,\{1,1\}}(t) = \frac{1}{32} + \frac{n_s(n_s-1)}{2}\frac{45}{64}t^2 U^1_{dd}\Big(q+\frac{3}{4}U^1_{dd}\Big), \tag{C9}$$

$$N^{(2)}_{\pm3,\{2,0\}}(t) = \frac{1}{32} + \frac{n_d(n_d-1)}{2}\frac{45}{32}t^2 \times \Big(U_1+\frac{1}{2}U^0_{dd}\Big)\Big(q+\frac{3}{4}U^0_{dd}\Big), \tag{C10}$$

where $U^0_{dd} = U_{dd}(\mathbf{0})$ is the on-site DDI and U^1_{dd} is the DDI to the neighboring site. In this derivation we neglected the U_2 and U_3 terms as their contribution is negligible.

2. Short-time dynamics at $O(t^4)$

In a double-well system, the t^4 contribution to the short-time dynamics is given by

$$N^{(4)}_m(t) = N^{(2)}_m(t) + \frac{t^4}{24}\big(p_1^2 A^m_1 + p_2^2 A^m_2 + p_1 p_2 A^m_{12}\big), \tag{C11}$$

where A^m_1, A^m_2, and A^m_{12} are the terms due to state with only singlons, only doublons, and the superposition of the two, respectively. Setting $m = 0$, we find

$$A^0_1 = \tfrac{45}{8}U^1_{dd}\big\{B^2\big(3q-2U^1_{dd}\big) + 4\big(q+\tfrac{3}{4}U^1_{dd}\big)\big[4q^2 + \tfrac{21}{4}qU^1_{dd} + \tfrac{37}{4}(U^1_{dd})^2\big]\big\} - 135J^2\big[\big(U_1+\tfrac{1}{2}U^0_{dd}\big)\big(2q+\tfrac{3}{4}U^0_{dd}\big) + \tfrac{1}{4}\big(-4q+3U_1+U^0_{dd}-\tfrac{5}{2}U^1_{dd}\big)U^1_{dd}\big], \tag{C12}$$

$$A^0_2 = \tfrac{45}{4}\big(U_1+\tfrac{1}{2}U^0_{dd}\big)\big(q+\tfrac{3}{4}U^0_{dd}\big)\big[2q\big(8q-3U_1+\tfrac{21}{2}U^0_{dd}\big) + 121U_1^2 + \tfrac{1}{2}U^0_{dd}\big(233U_1+74U^0_{dd}\big)\big] + 135J^2\big[\big(U_1+\tfrac{1}{2}U^0_{dd}\big)\big(2q+\tfrac{5}{4}U^0_{dd}\big) - \tfrac{1}{4}\big(4q-U_1+U^0_{dd}+\tfrac{3}{2}U^1_{dd}\big)U^1_{dd}\big], \tag{C13}$$

where we have used $B \equiv \gamma_B[b(\mathbf{r}_1) - b(\mathbf{r}_2)]$ for two nearest-neighboring sites at $\mathbf{r}_1$ and $\mathbf{r}_2$. If the double well starts in a superposition of $\{1,1\}$ (singlons) and $\{2,0\}$ (doublon-hole) states, then we get an additional contribution to the fourth-order dynamics given by

$$A^0_{12} = \tfrac{45}{4}J\big\{-B^2\big(U_1+\tfrac{1}{2}U^0_{dd}-U^1_{dd}\big) + 3U^0_{dd}\big(U_1+\tfrac{1}{2}U^0_{dd}\big) \times \big(2U_0+7U_1+8U^0_{dd}\big) + q\big[6U_0+43U_1 + 35\big(U^0_{dd}-U^1_{dd}\big)\big]\big(2U_1+U^0_{dd}-U^1_{dd}\big) + \tfrac{3}{2}U^1_{dd}\big[2U_0U_1+29U_1^2+3U_1U^0_{dd}-8(U^0_{dd})^2\big] - 3\big[U_0+13U_1+4\big(U^0_{dd}-U^1_{dd}\big)\big](U^1_{dd})^2\big\}. \tag{C14}$$

Similarly for the $m \pm 1$ we find

$$A^{\pm1}_1 = \tfrac{1}{4}A^0_1 + \tfrac{135}{4}U^1_{dd}\big(q-\tfrac{7}{2}U^1_{dd}\big)\big(q+\tfrac{3}{4}U^1_{dd}\big)^2, \tag{C15}$$

$$A^{\pm1}_2 = \tfrac{1}{4}A^0_2 + \tfrac{135}{4}\big(2q-17U_1-7U^0_{dd}\big) \times \big(U_1+\tfrac{1}{2}U^0_{dd}\big)\big(q+\tfrac{3}{4}U^0_{dd}\big)^2, \tag{C16}$$

and

$$A^{\pm1}_{12} = \tfrac{1}{4}A^0_{12}. \tag{C17}$$

The remaining terms are given by $A^{\pm2}_n = -\frac{1}{2}A^0_n$ and $A^{\pm3}_n = -A^{\pm1}_n$.

3. Divergence timescales

In the inset of Fig. 2(b) we see that the second-order results including doublons rapidly diverge from the exact simulation. To predict the timescales over which this divergence occurs,

we consider the largest term in the doublon expansion

$$\Delta N_0^{(2)} = -\frac{45(2\pi)^2 t^2}{8} U_1\left(q + 0.75 U_{dd}^0\right). \tag{C18}$$

The y axis in the inset covers $\Delta N_0 = 6 \times 10^{-5}$, and we find that $\Delta N_0^{(2)}$ changes by this amount in $t = 0.03$ ms, which agrees well with the figure. Divergence on an order of magnitude similar to that of the main figure (i.e., $\Delta N_0 = 0.15$) occurs when the higher-order terms become important. Considering the largest fourth-order term, which depends on tunneling, we get

$$\Delta N_0^{(4)} = \frac{135(2\pi)^4 t^4}{24} J^2 U_1 \left(2q + \frac{5}{4} U_{dd}^0 + \frac{1}{4} U_{dd}^1\right). \tag{C19}$$

Note that this predicts $\Delta N_0^{(4)} = 0.15$ at $t = 0.29$ ms, which indicates that the second-order results will break down for timescales on the order of $t = 0.29$ ms.

[1] C. Gross and I. Bloch, Science **357**, 995 (2017).
[2] I. Bloch, Nature (London) **453**, 1016 (2008).
[3] J. L. Bohn, A. M. Rey, and J. Ye, Science **357**, 1002 (2017).
[4] R. Blatt and C. F. Roos, Nat. Phys. **8**, 277 (2012).
[5] M. Gärttner, J. G. Bohnet, A. Safavi-Naini, M. L. Wall, J. J. Bollinger, and A. M. Rey, Nat. Phys. **13**, 781 (2017).
[6] J. G. Bohnet, B. C. Sawyer, J. W. Britton, M. L. Wall, A. M. Rey, M. Foss-Feig, and J. J. Bollinger, Science **352**, 1297 (2016).
[7] B. Neyenhuis, J. Zhang, P. W. Hess, J. Smith, A. C. Lee, P. Richerme, Z.-X. Gong, A. V. Gorshkov, and C. Monroe, Sci. Adv. **3**, e1700672 (2017).
[8] B. Yan, S. A. Moses, B. Gadway, J. P. Covey, K. R. A. Hazzard, A. M. Rey, D. S. Jin, and J. Ye, Nature (London) **501**, 521 (2013).
[9] K. R. A. Hazzard, B. Gadway, M. Foss-Feig, B. Yan, S. A. Moses, J. P. Covey, N. Y. Yao, M. D. Lukin, J. Ye, D. S. Jin, and A. M. Rey, Phys. Rev. Lett. **113**, 195302 (2014).
[10] H. Labuhn, D. Barredo, S. Ravets, S. de Léséleuc, T. Macrì, T. Lahaye, and A. Browaeys, Nature (London) **534**, 667 (2016).
[11] J. Zeiher, J.-y. Choi, A. Rubio-Abadal, T. Pohl, R. van Bijnen, I. Bloch, and C. Gross, Phys. Rev. X **7**, 041063 (2017).
[12] H. Bernien, S. Schwartz, A. Keesling, H. Levine, A. Omran, H. Pichler, S. Choi, A. S. Zibrov, M. Endres, M. Greiner, V. Vuletić, and M. D. Lukin, Nature (London) **551**, 579 (2017).
[13] D. Barredo, V. Lienhard, S. de Leseleuc, T. Lahaye, and A. Browaeys, Nature (London) **561**, 79 (2018).
[14] E. Guardado-Sanchez, P. T. Brown, D. Mitra, T. Devakul, D. A. Huse, P. Schauß, and W. S. Bakr, Phys. Rev. X **8**, 021069 (2018).
[15] S. Lepoutre, J. Schachenmayer, L. Gabardos, B. Zhu, B. Naylor, E. Marechal, O. Gorceix, A. M. Rey, L. Vernac, and B. Laburthe-Tolra, Nat. Commun. **10**, 1714 (2019).
[16] S. Baier, M. J. Mark, D. Petter, K. Aikawa, L. Chomaz, Z. Cai, M. Baranov, P. Zoller, and F. Ferlaino, Science **352**, 201 (2016).
[17] A. de Paz, P. Pedri, A. Sharma, M. Efremov, B. Naylor, O. Gorceix, E. Maréchal, L. Vernac, and B. Laburthe-Tolra, Phys. Rev. A **93**, 021603 (2016).
[18] A. de Paz, A. Sharma, A. Chotia, E. Maréchal, J. H. Huckans, P. Pedri, L. Santos, O. Gorceix, L. Vernac, and B. Laburthe-Tolra, Phys. Rev. Lett. **111**, 185305 (2013).
[19] Y. Tang, W. Kao, K.-Y. Li, S. Seo, K. Mallayya, M. Rigol, S. Gopalakrishnan, and B. L. Lev, Phys. Rev. X **8**, 021030 (2018).
[20] F. Böttcher, J.-N. Schmidt, M. Wenzel, J. Hertkorn, M. Guo, T. Langen, and T. Pfau, Phys. Rev. X **9**, 011051 (2019).
[21] L. Chomaz, R. M. W. van Bijnen, D. Petter, G. Faraoni, S. Baier, J. H. Becher, M. J. Mark, F. Wächtler, L. Santos, and F. Ferlaino, Nat. Phys. **14**, 442 (2018).
[22] M. A. Norcia, R. J. Lewis-Swan, J. R. K. Cline, B. Zhu, A. M. Rey, and J. K. Thompson, Science **361**, 259 (2018).
[23] E. J. Davis, G. Bentsen, L. Homeier, T. Li, and M. H. Schleier-Smith, Phys. Rev. Lett. **122**, 010405 (2019).
[24] T. Lahaye, C. Menotti, L. Santos, M. Lewenstein, and T. Pfau, Rep. Prog. Phys. **72**, 126401 (2009).
[25] D. Aharonov, D. Gottesman, S. Irani, and J. Kempe, Commun. Math. Phys. **287**, 41 (2009).
[26] S. Hallgren, D. Nagaj, and S. Narayanaswami, Quantum Inf. Comput. **13**, 721 (2013).
[27] A. Patscheider, B. Zhu, L. Chomaz, D. Petter, S. Baier, A. M. Rey, F. Ferlaino, and M. J. Mark, arXiv:1904.08262.
[28] T. Kimura, S. Tsuchiya, and S. Kurihara, J. Low Temp. Phys. **138**, 651 (2005).
[29] M. Yamashita and M. W. Jack, Phys. Rev. A **76**, 023606 (2007).
[30] S. Lepoutre, K. Kechadi, B. Naylor, B. Zhu, L. Gabardos, L. Isaev, P. Pedri, A. M. Rey, L. Vernac, and B. Laburthe-Tolra, Phys. Rev. A **97**, 023610 (2018).
[31] J. Schachenmayer, A. Pikovski, and A. M. Rey, Phys. Rev. X **5**, 011022 (2015).
[32] J. Schachenmayer, A. Pikovski, and A. M. Rey, New J. Phys. **17**, 065009 (2015).
[33] A. Polkovnikov, Ann. Phys. (NY) **325**, 1790 (2010).
[34] S. Lepoutre, L. Gabardos, K. Kechadi, P. Pedri, O. Gorceix, E. Maréchal, L. Vernac, and B. Laburthe-Tolra, Phys. Rev. Lett. **121**, 013201 (2018).
[35] Y. Kawaguchi and M. Ueda, Phys. Rep. **520**, 253 (2012).
[36] Y. Kawaguchi, H. Saito, K. Kudo, and M. Ueda, Phys. Rev. A **82**, 043627 (2010).
[37] M. Jreissaty, J. Carrasquilla, F. A. Wolf, and M. Rigol, Phys. Rev. A **84**, 043610 (2011).
[38] B. Zhu, A. M. Rey, and J. Schachenmayer, New J. Phys. **21**, 082001 (2019).
[39] Y. Liu, S. Jung, S. E. Maxwell, L. D. Turner, E. Tiesinga, and P. D. Lett, Phys. Rev. Lett. **102**, 125301 (2009).
[40] M. Jasperse, M. J. Kewming, S. N. Fischer, P. Pakkiam, R. P. Anderson, and L. D. Turner, Phys. Rev. A **96**, 063402 (2017).
[41] S. Palacios, S. Coop, P. Gomez, T. Vanderbruggen, Y. N. M. de Escobar, M. Jasperse, and M. W. Mitchell, New J. Phys. **20**, 053008 (2018).
[42] T. Fernholz, H. Krauter, K. Jensen, J. F. Sherson, A. S. Sørensen, and E. S. Polzik, Phys. Rev. Lett. **101**, 073601 (2008).
[43] S. Smale, P. He, B. Olsen, K. G. Jackson, H. Sharum, S. Trotzky, J. Marino, A. M. Rey, and J. H. Thywissen, Science Advances **5**, eaax1568 (2019).
[44] R. Asaoka, H. Tsuchiura, M. Yamashita, and Y. Toga, Phys. Rev. A **93**, 013628 (2016).